Research in Astron. Astrophys. **2011** Vol. **11** No. **5**, 524–536
http://www.raa-journal.org *http://www.iop.org/journals/raa*

Research in Astronomy and Astrophysics

Detailed study of B037 based on *HST* images *

Jun Ma
National Astronomical Observatories, Chinese Academy of Sciences, Beijing 100012, China; *majun@nao.cas.cn*
Key Laboratory of Optical Astronomy, National Astronomical Observatories, Chinese Academy of Sciences, Beijing 100012, China

Received 2010 September 1; accepted 2010 December 20

Abstract B037 is of interest because it is both the most luminous and the most highly reddened cluster known in M31. Deep observations and high spatial resolution images with the Advanced Camera for Surveys on the *Hubble Space Telescope (HST)* first showed that this cluster is crossed by a dust lane. Photometric data in the F606W and F814W filters obtained in this paper indicate that colors of $(\mathrm{F606W}-\mathrm{F814W})$ in the dust lane are redder ~ 0.4 mag than ones in the other regions of B037. The *HST* images show that this dust lane seems to be contained in B037, instead of in the M31 disk or the Milky Way. As far as we know, the formation of dust requires gas with a rather high metallicity. However, B037 has a low metallicity of $[\mathrm{Fe/H}] = -1.07 \pm 0.20$. So, it seems improbable that the observed dust lane is physically associated with B037. It is clear that the origin of this dust lane is worthy of future study. In addition, based on these images, we present the precise variation of ellipticity and position angle, and of surface brightness profile, and determine the structural parameters of B037 by fitting a single-mass isotropic King model. In the F606W filter, we derive the best-fitting scale radius $r_0 = 0.56 \pm 0.02''$ $(= 2.16 \pm 0.08\ \mathrm{pc})$, a tidal radius $r_\mathrm{t} = 8.6 \pm 0.4''$ $(= 33.1 \pm 1.5\,\mathrm{pc})$, and a concentration index $c = \log(r_\mathrm{t}/r_0) = 1.19 \pm 0.02$. In the F814W filter, we derive $r_0 = 0.56 \pm 0.01''$ $(= 2.16 \pm 0.04\ \mathrm{pc})$, $r_\mathrm{t} = 8.9 \pm 0.3''$ $(= 34.3 \pm 1.2\ \mathrm{pc})$, and $c = \log(r_\mathrm{t}/r_0) = 1.20 \pm 0.01$. The extinction-corrected central surface brightness is $\mu_0 = 13.53 \pm 0.03\,\mathrm{mag\ arcsec^{-2}}$ in the F606W filter, and $12.85 \pm 0.03\,\mathrm{mag\ arcsec^{-2}}$ in the F814W filter. We also calculate the half-light radius at $r_\mathrm{h} = 1.05 \pm 0.03''(= 4.04 \pm 0.12\,\mathrm{pc})$ in the F606W filter and $r_\mathrm{h} = 1.07 \pm 0.01''(= 4.12 \pm 0.04\ \mathrm{pc})$ in the F814W filter. In addition, we derived the complete magnitudes of B037 in the V and I bands by transforming the magnitudes from the ACS system to the standard system, which are in good agreement with previous ground-based broad-band photometry studies.

Key words: galaxies: evolution — galaxies: individual (M31) — globular cluster: individual (B037)

1 INTRODUCTION

Globular clusters (GCs) are effective laboratories for studying stellar evolution and stellar dynamics, and they are ancient building blocks of galaxies which can help us to understand the formation and

* Supported by the National Natural Science Foundation of China.

evolution of their parent galaxies. In addition, GCs exhibit surprisingly uniform properties, suggesting a common formation mechanism.

The closest other populous GC system beyond the halo of our Galaxy is that of M31. The study of M31 has been and continues to be a keystone of extragalactic astronomy (Barmby et al. 2000), and the study of GCs in M31 can be traced back to Hubble (1932). M31 GC B327 (B for 'Baade') or Bo37 (Bo for 'Bologna', see Battistini et al. 1987), which in the nomenclature introduced by Huchra et al. (1991) is referred to as B037, is a designation from the Revised Bologna Catalog (RBC) of M31 GCs and candidates (Galleti et al. 2004, 2006, 2007). The RBC is the main catalog used in studies of M31 GCs. The extremely red color of B037 was firstly noted by Kron & Mayall (1960), who suggested that this cluster must be highly reddened. Two years later, Vetešnik (1962b) determined magnitudes of 257 M31 GC candidates including B037 in the UBV photometric system. Then Vetešnik (1962a) studied the intrinsic colors of M31 GCs and found that B037 was the most highly reddened with $E(B-V)=1.28$ in his sample of M31 GC candidates based on the photometric catalog of Vetešnik (1962b). With low-resolution spectroscopy, Crampton et al. (1985) also found that B037 is the most highly reddened GC candidate in M31 to have $E(B-V)=1.48$. Based on a large database of multicolor photometry, Barmby et al. (2000) determined the reddening value for each individual M31 GC including B037 using the correlations between optical and infrared colors and metallicity by defining various "reddening-free" parameters. The reddening value of B037 is $E(B-V)=1.38\pm0.02$ (which is kindly given to us by P. Barmby). Again, Barmby et al. (2002b) derived the reddening value for this cluster to be $E(B-V)=1.30\pm0.04$, using the spectroscopic metallicity to predict the intrinsic colors. Ma et al. (2006a) also determined the reddening of B037 to be $E(B-V)=1.360\pm0.013$ by comparing the independently obtained multicolor photometry with theoretical stellar population synthesis models, which is in good agreement with the other results. Following the methods of Barmby et al. (2000), Fan et al. (2008) (re-)determined reddening values for 443 clusters and cluster candidates including B037, and the redding value of B037 obtained by Fan et al. (2008) is $E(B-V)=1.21\pm0.03$, which is a little smaller than the previous determinations.

The brightest GCs in M31 are more luminous than the brightest Galactic cluster, ω Centauri. Among these are B037 (van den Bergh 1968) and G1 (see details from Barmby et al. 2002b). These two clusters are both considered as possible remnant cores of a former dwarf galaxy which lost most of its envelope through tidal interactions with M31 (Meylan & Heggie 1997; Meylan et al. 2001; Mackey & van den Bergh 2005; Ma et al. 2006b, 2007).

In this paper, we will present the photometric data of B037 using deep images obtained with the Advanced Camera for Surveys (ACS) on the *HST*. The deep images with high spatial resolution show that this cluster is crossed by a dust lane. Our results demonstrate that colors of F814W$-$F606W in the dust lane are redder by ~ 0.4 mag than ones from the other regions. In addition, we studied structures of B037 in detail based on these images.

2 OBSERVATIONS AND DATA REDUCTION

2.1 *HST* Images of B037

We searched the *HST* archive and found B037 to have been observed with the ACS-Wide Field Channel (WFC) in the F606W and the F814W filters, which were observed on 2004 August 2 and on 2004 July 4, respectively. The exposure time was 2370.0 seconds for both bands. The *HST* ACS-WFC resolution was $0.05''$ per pixel. The images in F606W and F814W both show that B037 is crossed by a dust lane. Figure 1 clearly shows the dust lane, which crosses B037. If the dust lane is really part of B037, its color should be different from that in other regions.

Unless stated otherwise, the magnitudes are always given in the VEGAMAG scale as defined by Sirianni et al. (2005). The relevant zero-point for this system is 26.398 and 25.501 for WFC F606W

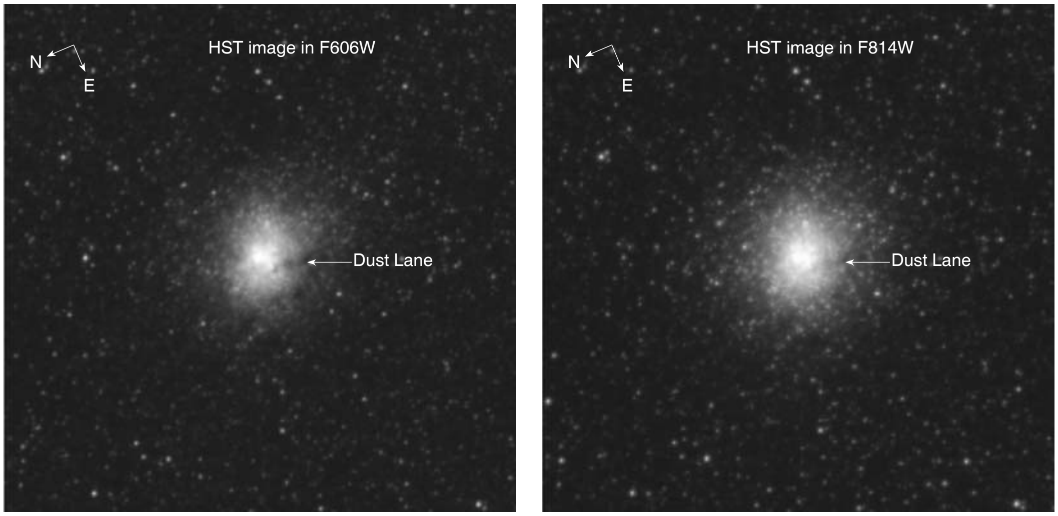

Fig. 1 Images of GC B037 observed in the F606W and F814W filters of ACS/*HST*. The images clearly show that the cluster is crossed by a dust lane. The image size is $17.5'' \times 17.5''$ for each panel.

Table 1 Photometric Data for B037

Source No.	F606W (mag)	F814W (mag)	F606W−F814W (mag)
1	23.29 ± 0.26	21.35 ± 0.16	1.94
2	23.03 ± 0.23	21.14 ± 0.15	1.89
3	22.95 ± 0.22	21.00 ± 0.14	1.95
4	23.22 ± 0.25	21.25 ± 0.15	1.97
5	23.17 ± 0.25	21.36 ± 0.16	1.81
6	21.15 ± 0.10	19.10 ± 0.06	2.05
7	22.93 ± 0.22	20.53 ± 0.11	2.40
8	23.41 ± 0.28	20.94 ± 0.13	2.47
9	24.66 ± 0.49	22.31 ± 0.25	2.35

and WFC F814W, respectively. The distance to M31 of 780 kpc ($1''$ subtends 3.8 pc) is adopted in this paper.

2.2 Color Difference Between the Dust Lane and the Other Regions

In order to study whether a color difference between the dust lane and the other regions in B037 really exists, we select nine points, three of which (Nos. 7, 8 and 9) are located in the dust lane, while the other six are randomly located in other regions (see Fig. 2). For each sample point, the PHOT routine in DAOPHOT (Stetson 1987) is used to obtain the magnitude. We adopt an aperture with a diameter of four pixels. The photometric data for these nine sample points are given in Table 1, in conjunction with the 1σ magnitude uncertainties from DAOPHOT. Column 4 gives the color of (F606W − F814W). From Table 1, we can see that colors of (F606W − F814W) in the dust lane are redder than ones in the other regions by ~ 0.4 mag.

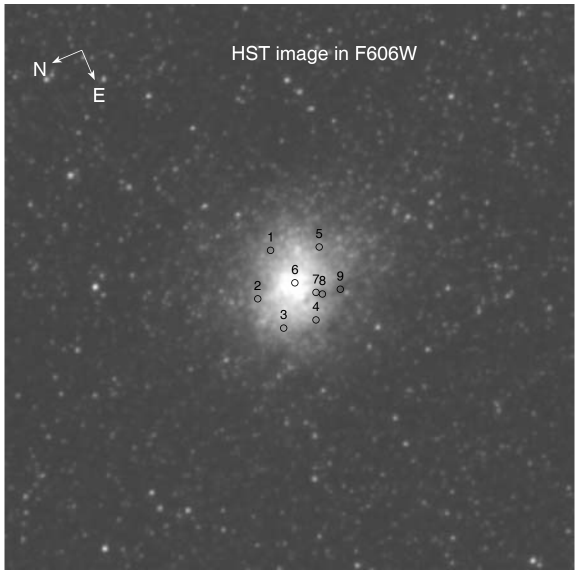

Fig. 2 Sample positions of photometry (black circles) are shown in the image of GC B037 observed in the F606W filter of ACS/*HST*. An aperture with a radius of two pixels is adopted for photometry. The image size is $17.5'' \times 17.5''$.

2.3 Surface Brightness Profiles

We used the *IRAF* task *ELLIPSE* to obtain F606W and F814W surface brightness profiles for B037. B037's center position was fixed at a value derived by the object locator of the *ELLIPSE* task, however an initial center position was determined by computing the centroid. Elliptical isophotes were fitted to the data, with no sigma clipping. We ran two passes of the *ELLIPSE* task. The first pass was run in the usual way, with ellipticity and position angle being allowed to vary with the isophote's semimajor axis. In the second pass, surface brightness profiles on fixed, zero-ellipticity isophotes were measured, since we chose to fit circular models for the intrinsic cluster structure and the point spread function (PSF) as Barmby et al. (2007) did (see Sect. 2.4 for details). The background value was derived as the mean of a region containing 100×100 pixels in "empty" areas far away from the cluster.

2.3.1 Ellipticity and position angle

Tables 2 and 3 give the ellipticity, $\epsilon = 1 - b/a$, and the position angle (P.A.) as a function of the semi-major axis length, a, from the center of the annulus in the F606W and F814W filter bands, respectively. These observables have also been plotted in Figures 3 and 4, respectively; the errors were generated by the IRAF task ELLIPSE, in which the ellipticity errors are obtained from the internal errors in the harmonic fit, after removal of the first and second fitted harmonics. From Table 3, and Figures 3 and 4, we can see that the values of ellipticity and position angle cannot be obtained within $0.1448''$ in the F814W filter because of very high ellipticity (> 1.0). Ma et al. (2006b) analyzed the same F606W image that B037 used here, fitting a King (1962) model to a surface brightness profile made from a PSF-deconvolved image. They also plotted the distributions of ellipticity and position angle as a function of the semi-major axis length. Comparison between fig. 2 of Ma et al. (2006b) and Figures 3 and 4 shows that the general trend of the cluster's ellipticity as a function of semimajor axis radius is similar between Ma et al. (2006b) and the present paper. The comparison also shows that uncertainties in the exact value of the PA are only of secondary importance with respect to the general trend in observed ellipticity, given that the PA determination between Ma et al. (2006b) and the present paper differs rather significantly. There are a number of possible reasons for the offsets in PA observed between these two studies. The main reason is that Ma et al. (2006b) used the PSF-deconvolved image. Other reasons include those related to the positions of the centering of isophotes and the different geometrical parameters set when fitting. In addition, Figure 3 shows that the ellipticity varies significantly with position along the cluster's semimajor axis, especially for values smaller than $0.5''$. In the F814W filter band, the ellipticity is larger than 1.0 along the cluster's semimajor axis for values smaller than $0.1448''$.

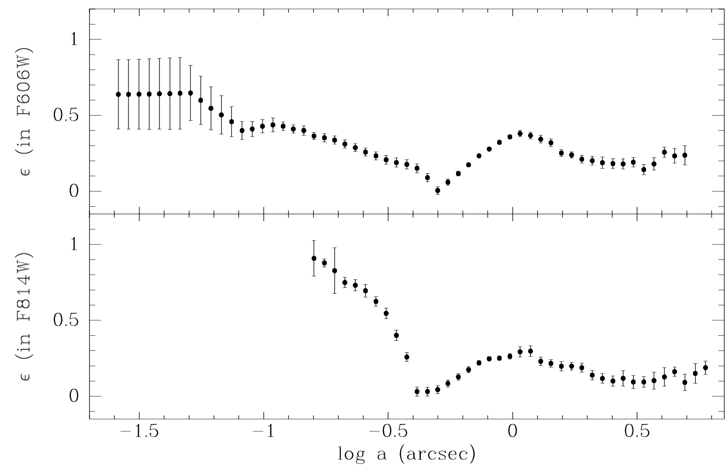

Fig. 3 Ellipticity as a function of semimajor axis in the F606W and F814W filters of ACS/*HST*.

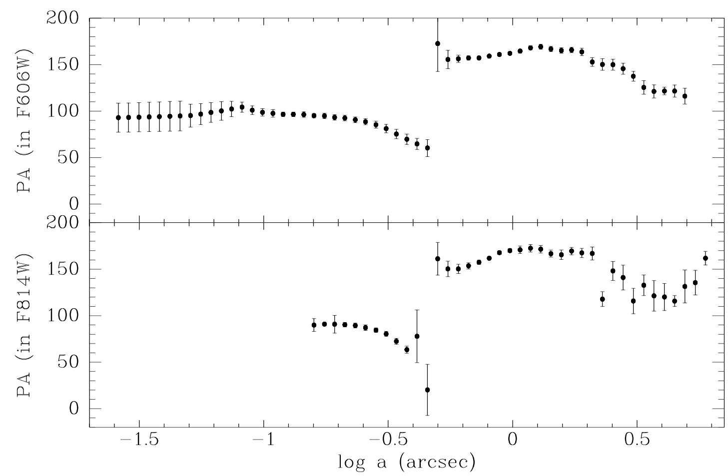

Fig. 4 P.A. as a function of semimajor axis in the F606W and F814W filters of ACS/*HST*.

Table 2 B037: Ellipticity, ϵ, and position angle (P.A.) as a function of semimajor axis, a, in the F606W filter of *HST* ACS-WFC.

a (arcsec)	ϵ	P.A. (°)	a (arcsec)	ϵ	P.A. (°)
0.0260	0.638 ± 0.228	92.9 ± 15.5	0.3757	0.177 ± 0.031	69.8 ± 5.6
0.0287	0.638 ± 0.229	93.2 ± 15.6	0.4132	0.151 ± 0.029	64.7 ± 5.9
0.0315	0.639 ± 0.230	93.4 ± 15.7	0.4545	0.090 ± 0.027	60.3 ± 9.1
0.0347	0.640 ± 0.232	93.7 ± 15.8	0.5000	0.005 ± 0.025	172.6 ± 30.0
0.0381	0.642 ± 0.233	94.0 ± 15.9	0.5500	0.060 ± 0.020	155.5 ± 9.8
0.0420	0.643 ± 0.235	94.4 ± 16.0	0.6050	0.117 ± 0.015	156.3 ± 3.9
0.0461	0.645 ± 0.236	94.7 ± 16.0	0.6655	0.174 ± 0.012	157.2 ± 2.2
0.0508	0.647 ± 0.182	95.2 ± 12.3	0.7321	0.233 ± 0.011	157.2 ± 1.5
0.0558	0.599 ± 0.159	96.8 ± 11.2	0.8053	0.278 ± 0.011	159.1 ± 1.3
0.0614	0.546 ± 0.142	98.5 ± 10.6	0.8858	0.322 ± 0.011	160.8 ± 1.1
0.0676	0.503 ± 0.127	100.2 ± 10.0	0.9744	0.358 ± 0.012	162.1 ± 1.2
0.0743	0.458 ± 0.099	102.2 ± 8.3	1.0718	0.380 ± 0.021	164.5 ± 2.1
0.0818	0.400 ± 0.059	104.3 ± 5.5	1.1790	0.367 ± 0.022	168.0 ± 2.2
0.0899	0.410 ± 0.050	101.0 ± 4.6	1.2969	0.343 ± 0.025	169.2 ± 2.7
0.0989	0.428 ± 0.044	98.7 ± 3.9	1.4266	0.319 ± 0.025	166.8 ± 2.8
0.1088	0.437 ± 0.046	97.6 ± 3.9	1.5692	0.252 ± 0.022	165.1 ± 3.0
0.1197	0.428 ± 0.028	96.6 ± 2.5	1.7261	0.239 ± 0.021	165.7 ± 2.9
0.1317	0.410 ± 0.027	96.5 ± 2.5	1.8987	0.211 ± 0.026	163.6 ± 4.0
0.1448	0.400 ± 0.031	96.3 ± 3.0	2.0886	0.201 ± 0.029	152.8 ± 4.6
0.1593	0.364 ± 0.023	95.1 ± 2.3	2.2975	0.188 ± 0.037	150.1 ± 6.3
0.1752	0.352 ± 0.027	94.8 ± 2.8	2.5272	0.182 ± 0.033	149.9 ± 5.8
0.1928	0.337 ± 0.027	93.2 ± 2.9	2.7800	0.180 ± 0.034	145.6 ± 6.0
0.2120	0.311 ± 0.027	92.5 ± 3.0	3.0580	0.191 ± 0.031	137.5 ± 5.2
0.2333	0.287 ± 0.026	90.6 ± 3.1	3.3638	0.143 ± 0.034	125.4 ± 7.2
0.2566	0.258 ± 0.026	88.6 ± 3.3	3.7001	0.180 ± 0.041	121.1 ± 7.1
0.2822	0.233 ± 0.027	85.4 ± 3.8	4.0701	0.257 ± 0.033	121.6 ± 4.1
0.3105	0.207 ± 0.029	81.2 ± 4.5	4.4772	0.233 ± 0.048	121.6 ± 6.5
0.3415	0.189 ± 0.030	75.3 ± 5.0	4.9249	0.237 ± 0.063	116.1 ± 8.5

2.4 Point Spread Function

At a distance of 780 kpc, the ACS/WFC has a scale of $0.05\ \mathrm{arcsec} = 0.19\ \mathrm{pc\ pixel}^{-1}$, and thus M31 clusters are clearly resolved within it. Their observed core structures, however, are still affected by the PSF. We chose not to deconvolve the data, but instead fit structural models after convolving them with a simple analytic description of the PSF as Barmby et al. (2007) did. To estimate the PSF for the WFC, Barmby et al. (2007) used the *IRAF* task *ELLIPSE* with circular symmetry enforced to produce intensity profiles out to radii of about $2''$(40 pixels) for a number of isolated stars on a number of images, and combined them to produce a single, average PSF. This was done separately for the F606W and F814W filters. They originally tried to fit these with simple Moffat profiles (with backgrounds added), but found that a better description was given by a function of the form below. For the combination of the WFC and F606W filter,

$$I_{\mathrm{PSF}} = I_0 \left[1 + (R/0.0686'')^3\right]^{-1.23}, \tag{1}$$

which has a full width at half-maximum of $\mathrm{FWHM} = 0.125''$, or about 2.5 pixels; for the combination of the WFC and F814W filter,

$$I_{\mathrm{PSF}} = I_0 \left[1 + (R/0.0783'')^3\right]^{-1.19}, \tag{2}$$

Table 3 B037: Ellipticity, ϵ, and position angle (P.A.) as a function of semimajor axis, a, in the F814W filter of *HST* ACS-WFC.

a (arcsec)	ϵ	P.A. ($^\circ$)	a (arcsec)	ϵ	P.A. ($^\circ$)
0.0260			0.4132	0.031 ± 0.030	77.8 ± 28.3
0.0287			0.4545	0.031 ± 0.029	20.2 ± 27.5
0.0315			0.5000	0.044 ± 0.027	161.2 ± 17.6
0.0347			0.5500	0.084 ± 0.023	150.3 ± 8.3
0.0381			0.6050	0.127 ± 0.021	150.3 ± 5.0
0.0420			0.6655	0.175 ± 0.019	153.6 ± 3.4
0.0461			0.7321	0.220 ± 0.016	157.4 ± 2.3
0.0508			0.8053	0.247 ± 0.013	161.8 ± 1.7
0.0558			0.8858	0.251 ± 0.014	167.8 ± 1.8
0.0614			0.9744	0.263 ± 0.017	170.0 ± 2.1
0.0676			1.0718	0.293 ± 0.034	170.8 ± 4.0
0.0743			1.1790	0.297 ± 0.035	172.5 ± 4.1
0.0818			1.2969	0.230 ± 0.028	171.5 ± 4.0
0.0899			1.4266	0.216 ± 0.025	166.7 ± 3.7
0.0989			1.5692	0.198 ± 0.031	165.5 ± 5.1
0.1088			1.7261	0.198 ± 0.025	169.5 ± 4.0
0.1197			1.8987	0.188 ± 0.029	167.5 ± 5.0
0.1317			2.0886	0.139 ± 0.031	166.9 ± 6.9
0.1448			2.2975	0.117 ± 0.031	117.8 ± 8.0
0.1593	0.908 ± 0.117	89.9 ± 6.9	2.5272	0.100 ± 0.034	148.1 ± 10.2
0.1752	0.878 ± 0.026	90.9 ± 1.5	2.7800	0.118 ± 0.051	141.0 ± 13.3
0.1928	0.827 ± 0.151	90.8 ± 9.6	3.0580	0.094 ± 0.043	115.8 ± 13.7
0.2120	0.749 ± 0.034	90.3 ± 2.3	3.3638	0.094 ± 0.035	132.7 ± 11.1
0.2333	0.731 ± 0.037	89.4 ± 2.6	3.7001	0.103 ± 0.056	121.3 ± 16.4
0.2566	0.695 ± 0.041	87.1 ± 2.9	4.0701	0.127 ± 0.061	120.1 ± 14.6
0.2822	0.624 ± 0.031	84.4 ± 2.3	4.4772	0.162 ± 0.031	115.7 ± 5.9
0.3105	0.546 ± 0.035	80.4 ± 2.6	4.9249	0.091 ± 0.054	131.4 ± 17.7
0.3415	0.401 ± 0.035	72.4 ± 3.2	5.4174	0.150 ± 0.065	135.5 ± 13.3
0.3757	0.258 ± 0.029	63.4 ± 3.8	5.9591	0.188 ± 0.044	161.8 ± 7.4

which has a full width at half-maximum of $\mathrm{FWHM} = 0.145''$, or about 2.9 pixels. In addition, since this PSF formula is radially symmetric and the models of King (1966) which we fit are intrinsically spherical, the convolved models to be fitted to the data are also circularly symmetric.

2.5 Extinction

When we fit models to the brightness profiles of B037, we will correct the inferred magnitude parameters for extinction. The reddening law from Cardelli et al. (1989) is employed in this paper. The effective wavelengths of the ACS F606W and F814W filters are $\lambda_{\rm eff} = 5918$ and 8060 Å respectively (Sirianni et al. 2005), so that from Cardelli et al. (1989), $A_{\rm F606W} \simeq 2.8 \times E(B-V)$ and $A_{\rm F814W} \simeq 1.8 \times E(B-V)$ (see Barmby et al. 2007; McLaughlin et al. 2008, for details). The reddening value of $E(B-V) = 1.360 \pm 0.013$ from Ma et al. (2006a) is adopted in this paper.

2.6 Magnitudes of B037 in F606W and F814W Filters

We derived the total flux of B037 in F606W and F814W filter bands using the *IRAF* task *PHOT* in *DAPPHOT* as below: measuring aperture magnitudes in concentric apertures with an interval of $0.1''$, drawing magnitude growth curves, and paying attention to where the flux does not increase. Finally, we obtained the magnitudes of B037 in F606W and F814W to be 16.21 ± 0.010 and 14.16 ± 0.006, respectively. In the photometry, we derived the background value as the mean of a region far away from the cluster (see Sect. 2.3 for details). We use the VEGAMAG photometric system. In order to allow for a meaningful comparison with the previous ground-based broad-band photometry of Barmby et al. (2000), we transformed the magnitudes from the ACS system to the standard broad-band photometric system by following the transformation equations and coefficients of table 22 of Sirianni et al. (2005). The results are $m_V(\mathrm{ACS}) = 16.83$ (this paper) versus $m_V = 16.82$ (Barmby et al. 2000), and $m_I(\mathrm{ACS}) = 14.15$ (this paper) versus $m_I = 14.16$ (Barmby et al. 2000). Our results are in good agreement with Barmby et al. (2000).

3 MODELS AND FITS

3.1 Structural Models

Besides elliptical galaxies, GCs are the best understood and most thoroughly modeled class of stellar systems. For example, a large majority of the $\sim$150 Galactic GCs have been fitted by the simple models of single-mass, isotropic, lowered isothermal spheres developed by Michie (1963) and King (1966) (hereafter "King models"), yielding comprehensive catalogs of cluster structural parameters and physical properties (see McLaughlin & van der Marel 2005, and references therein). For extragalactic GCs, *HST* imaging data have been used to fit King models to a large number of GCs in M31 (e.g., Barmby et al. 2002a, 2007, and references therein), in M33 (Larsen et al. 2002), and in NGC 5128 (e.g., Harris et al. 2002; McLaughlin et al. 2008, and references therein). In this paper, we fit the usual King models to the density profile of B037 observed with ACS/WFC.

3.2 Observed Data

Tables 4 and 5 list the surface brightness, μ, of B037, and its integrated magnitude, m, as a function of radius in the F606W and F814W filters, respectively. The errors in the surface brightness were also generated by the *IRAF* task *ELLIPSE*, in which they were obtained directly from the root mean square scatter of the intensity data along the zero-ellipticity isophotes. In addition, the surface photometries at radii where the ellipticity and position angle cannot be measured are obtained based on the last ellipticity and position angle, which is how the *IRAF* task *ELLIPSE* is designed.

3.3 Fits

Our fitting procedure involves computing large numbers of King structural models, spanning a wide range of fixed values of the appropriate shape parameter W_0 (see McLaughlin & van der Marel 2005, for details). Then the models are convolved with the ACS/WFC PSF for the F606W and F814W filters of Equations (1) and (2)

$$\widetilde{I}^{*}_{\mathrm{mod}}(R|r_0) = \iint_{-\infty}^{\infty} \widetilde{I}_{\mathrm{mod}}(R'/r_0) \times \widetilde{I}_{\mathrm{PSF}}\left[(x-x'),(y-y')\right]\, dx'\, dy'\,, \tag{3}$$

where $\widetilde{I}_{\mathrm{mod}} \equiv I_{\mathrm{mod}}/I_0$, and $\widetilde{I}_{\mathrm{PSF}}$ is the PSF profile normalized to unit total luminosity (see McLaughlin et al. 2008, for details). We changed the luminosity density to surface brightness $\widetilde{\mu}^{*}_{\mathrm{mod}} = -2.5\,\log[\widetilde{I}^{*}_{\mathrm{mod}}]$ before fitting them to the observed surface-brightness profile of B037, $\mu = \mu_0 - 2.5\,\log[I(R/r_0)/I_0]$, finding the radial scale r_0 and central surface brightness μ_0 which minimize χ^2 for every given value of W_0. The (W_0, r_0, μ_0) combination that yielded the global minimum χ^2_{min} over the grid used the best-fit model of that type.

$$\chi^2 = \sum_i \frac{\left[\mu_{\mathrm{obs}}(R_i) - \widetilde{\mu}^{*}_{\mathrm{mod}}(R_i|r_0)\right]^2}{\sigma_i^2}, \tag{4}$$

Table 4 B037: Surface brightness, μ, and integrated magnitude, m, as a function of radius in the F606W filter of *HST* ACS-WFC.

R (arcsec)	μ (mag)	m (mag)	R (arcsec)	μ (mag)	m (mag)
0.0260	17.327 ± 0.007	23.827	0.3757	17.792 ± 0.040	18.456
0.0287	17.328 ± 0.008	23.827	0.4132	17.863 ± 0.046	18.264
0.0315	17.328 ± 0.008	23.827	0.4545	17.944 ± 0.049	18.123
0.0347	17.329 ± 0.009	23.827	0.5000	18.040 ± 0.049	17.962
0.0381	17.330 ± 0.010	23.827	0.5500	18.148 ± 0.048	17.827
0.0420	17.331 ± 0.011	23.827	0.6050	18.267 ± 0.048	17.672
0.0461	17.331 ± 0.012	23.827	0.6655	18.389 ± 0.053	17.549
0.0508	17.332 ± 0.014	22.086	0.7321	18.495 ± 0.061	17.414
0.0558	17.334 ± 0.015	22.086	0.8053	18.598 ± 0.070	17.295
0.0614	17.338 ± 0.016	22.086	0.8858	18.716 ± 0.077	17.165
0.0676	17.341 ± 0.018	22.086	0.9744	18.854 ± 0.079	17.039
0.0743	17.346 ± 0.020	21.452	1.0718	19.006 ± 0.077	16.927
0.0818	17.351 ± 0.022	21.452	1.1790	19.193 ± 0.107	16.822
0.0899	17.356 ± 0.024	21.452	1.2969	19.440 ± 0.105	16.731
0.0989	17.363 ± 0.027	21.452	1.4266	19.721 ± 0.116	16.642
0.1088	17.372 ± 0.027	21.062	1.5692	20.001 ± 0.113	16.570
0.1197	17.382 ± 0.029	20.552	1.7261	20.293 ± 0.116	16.505
0.1317	17.395 ± 0.028	20.552	1.8987	20.597 ± 0.122	16.451
0.1448	17.411 ± 0.028	20.370	2.0886	20.872 ± 0.128	16.401
0.1593	17.429 ± 0.029	19.964	2.2975	21.224 ± 0.105	16.358
0.1752	17.450 ± 0.028	19.964	2.5272	21.457 ± 0.112	16.320
0.1928	17.475 ± 0.026	19.764	2.7800	21.719 ± 0.138	16.283
0.2120	17.504 ± 0.026	19.528	3.0580	22.082 ± 0.154	16.251
0.2333	17.538 ± 0.025	19.337	3.3638	22.603 ± 0.164	16.225
0.2566	17.578 ± 0.026	19.091	3.7001	23.042 ± 0.225	16.206
0.2822	17.624 ± 0.026	19.009	4.0701	23.694 ± 0.467	16.191
0.3105	17.675 ± 0.030	18.802	4.4772	24.509 ± 0.571	16.182
0.3415	17.732 ± 0.034	18.634	4.9249	25.173 ± 1.342	16.172

in which σ_i is the error in the surface brightness. Estimates of the one-sigma uncertainties on these basic fit parameters follow from their extreme values over the subgrid of fits with $\chi^2/\nu \leq \chi^2_{\rm min}/\nu + 1$, where ν is the number of free parameters. Figure 5 shows our best King fits to B037. In Figure 5, open squares are ELLIPSE data points included in the least-squares model fitting, and the asterisks are points not used to constrain the fit. These observed data points shown by asterisks are included in the radius of $R < 2$ pixels $= 0.1''$, and the isophotal intensity is dependent on its neighbors. As Barmby et al. (2007) pointed out, the ELLIPSE output contains brightnesses for 15 radii inside 2 pixels, but they are all measured from the same 13 central pixels and are not statistically independent. So, to avoid excessive weighting of the central regions of B037 in the fits, we only used intensities at radii $R_{\rm min}$, $R_{\rm min} + (0.5, 1.0, 2.0\ \rm pixels)$, or $R > 2.5$ pixels as Barmby et al. (2007) used. Table 6 summarizes the results obtained in this paper.

3.4 Comparison to Previous Results

Ma et al. (2006b) analyzed the same F606W image of B037 used here, fitting a King (1962) model to a surface brightness profile derived from a PSF-deconvolved image. They derived the scale radius $r_0 = 0.72''$ (it is called the core radius in Ma et al. (2006b)), half-light radius $r_{\rm h} = 1.11''$, concentration index $c = 0.91$, and central surface brightness $\mu(0) = 17.21\ \rm mag\ arcsec^{-2}$ (using the value for extinction adopted in this paper, this becomes $\mu_0 = 13.40\ \rm mag\ arcsec^{-2}$). Comparing the results of Ma et al. (2006b) with Table 6 of this paper, we find that our model fits produce a

Table 5 B037: Surface brightness, μ, and integrated magnitude, m, as a function of radius in the F814W filter of *HST* ACS-WFC.

R (arcsec)	μ (mag)	m (mag)	R (arcsec)	μ (mag)	m (mag)
0.0260	15.301 ± 0.010	21.800	0.4132	15.772 ± 0.032	16.190
0.0287	15.302 ± 0.011	21.800	0.4545	15.863 ± 0.036	16.048
0.0315	15.303 ± 0.012	21.800	0.5000	15.967 ± 0.038	15.889
0.0347	15.303 ± 0.013	21.800	0.5500	16.078 ± 0.037	15.754
0.0381	15.304 ± 0.015	21.800	0.6050	16.190 ± 0.033	15.598
0.0420	15.305 ± 0.016	21.800	0.6655	16.300 ± 0.036	15.474
0.0461	15.306 ± 0.018	21.800	0.7321	16.407 ± 0.046	15.338
0.0508	15.308 ± 0.019	20.061	0.8053	16.543 ± 0.053	15.218
0.0558	15.310 ± 0.021	20.061	0.8858	16.706 ± 0.054	15.094
0.0614	15.313 ± 0.024	20.061	0.9744	16.847 ± 0.054	14.974
0.0676	15.317 ± 0.026	20.061	1.0718	16.995 ± 0.061	14.868
0.0743	15.321 ± 0.030	19.430	1.1790	17.185 ± 0.105	14.767
0.0818	15.326 ± 0.033	19.430	1.2969	17.459 ± 0.086	14.681
0.0899	15.331 ± 0.037	19.430	1.4266	17.717 ± 0.107	14.596
0.0989	15.337 ± 0.041	19.430	1.5692	18.006 ± 0.101	14.527
0.1088	15.347 ± 0.043	19.039	1.7261	18.279 ± 0.102	14.464
0.1197	15.360 ± 0.043	18.531	1.8987	18.567 ± 0.086	14.411
0.1317	15.367 ± 0.045	18.531	2.0886	18.833 ± 0.092	14.359
0.1448	15.375 ± 0.048	18.350	2.2975	19.167 ± 0.095	14.316
0.1593	15.396 ± 0.046	17.940	2.5272	19.460 ± 0.094	14.277
0.1752	15.411 ± 0.046	17.940	2.7800	19.649 ± 0.156	14.240
0.1928	15.428 ± 0.045	17.738	3.0580	20.075 ± 0.137	14.207
0.2120	15.447 ± 0.046	17.496	3.3638	20.538 ± 0.103	14.181
0.2333	15.466 ± 0.048	17.301	3.7001	21.002 ± 0.138	14.160
0.2566	15.501 ± 0.046	17.046	4.0701	21.399 ± 0.203	14.142
0.2822	15.531 ± 0.043	16.960	4.4772	21.964 ± 0.228	14.129
0.3105	15.580 ± 0.037	16.745	4.9249	22.519 ± 0.240	14.117
0.3415	15.632 ± 0.031	16.573	5.4174	23.311 ± 0.588	14.106
0.3757	15.695 ± 0.029	16.388	5.9591	23.508 ± 0.782	14.096

Table 6 Structural Parameters of B037

Parameter	F606W	F814W
r_0	$0.56 \pm 0.02''$ $(= 2.16 \pm 0.08$ pc)	$0.56 \pm 0.01''$ $(= 2.16 \pm 0.04$ pc)
$r_{\rm t}$	$8.6 \pm 0.4''$ $(= 33.1 \pm 1.5$ pc)	$8.9 \pm 0.3''$ $(= 34.3 \pm 1.2$ pc)
$c = \log(r_{\rm t}/r_0)$	1.19 ± 0.02	1.20 ± 0.01
$r_{\rm h}$	$1.05 \pm 0.03''(= 4.04 \pm 0.12$ pc)	$1.07 \pm 0.01''(= 4.12 \pm 0.04$ pc)
μ_0 (mag arcsec^{-2})	13.53 ± 0.03	12.85 ± 0.03

somewhat higher concentration and smaller scale radius. These differences come from: (i) using different models (King 1962 vs. King 1966) (ii) the observed data are obtained in different ways. In (ii), Ma et al. (2006b) derived the surface brightness profile from a PSF-deconvolved image; in addition, Ma et al. (2006b) derived the surface brightness profile with ellipticity and position angle allowed to vary with the isophote's semimajor axis. However, in this paper, we derived the surface brightness profile on fixed, zero-ellipticity isophotes, since we chose to fit circular models for the intrinsic cluster structure and the PSF as Barmby et al. (2007) did (see Sect. 2.4 for details). In fact, from Figure 5 of this paper and figure 3 of Ma et al. (2006b), we can see that the observed data are somewhat different between Ma et al. (2006b) and this paper.

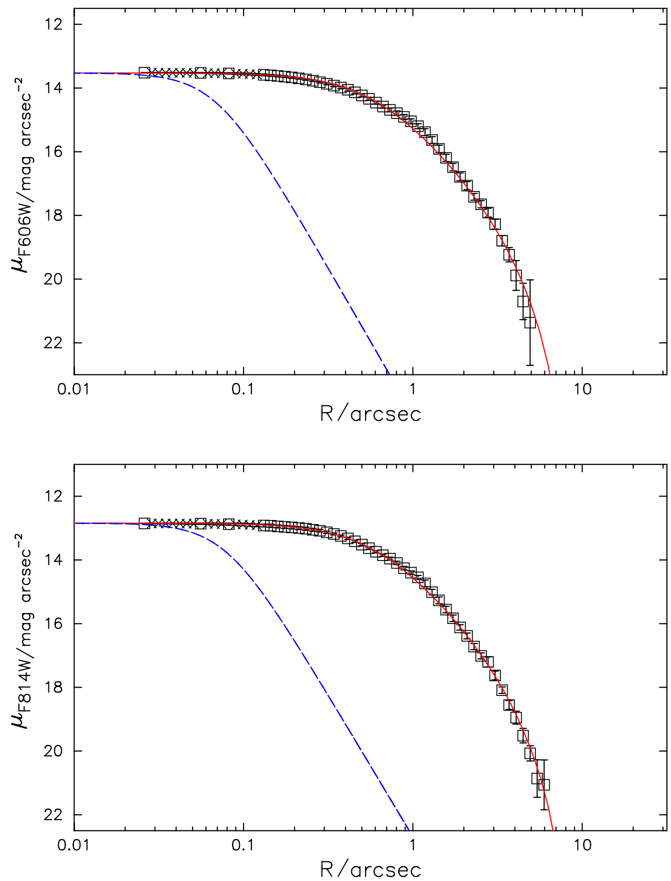

Fig. 5 Surface brightness profile of B037 measured in the F606W and F814 filters. Dashed curves (*blue*) trace the PSF intensity profiles and solid (*red*) curves (color online) are the PSF-convolved best-fit models. Open squares are ELLIPSE data points included in the χ^2 model fitting, and the asterisks are points not used to constrain the fits (see the text for details).

Barmby et al. (2007) analyzed the same F606W and F814W images of B037 used here with nearly the same observed data and method. The results of comparison are listed in Table 7 (table 5 of Barmby et al. 2007, in the electronic edition, did not list the results of B037 in the F814W filter), from which we can see that the results obtained in this paper are in good agreement with ones of Barmby et al. (2007) (about the central surface brightnesses, we have corrected them using the value for extinction adopted in this paper).

4 DISCUSSION AND SUMMARY

As discussed in Section 3.1, it is impossible for the dust lane to come from the Milky Way. Another possibility is that the dust lane is contained in B037 itself. As far as we know, the formation of dust requires gas with a rather high metallicity. Perrett et al. (2002) presented metallicities for more than 200 GCs in M31, including B037, using the Wide Field Fibre Optic Spectrograph at the 4.2 m William Herschel Telescope in La Palma, Canary Islands, which provides a total spectral coverage of $\sim$ 3700–5600 Å with two gratings. One grating (H2400B 2400 line) yielded a dispersion of

Table 7 Results of Comparison

	F606W		F814W	
Parameter	Barmby et al. (2007)	This paper	Barmby et al. (2007)	This paper
r_0 ($''$)	0.56	0.56	0.59	0.56
$c = \log(r_\mathrm{t}/r_0)$	1.23	1.19	1.18	1.20
r_h ($''$)	1.09	1.05	—	1.07
μ_0 (mag arcsec^{-2})	13.45	13.53	12.75	12.85

0.8 Å pixel^{-1} and a spectral resolution of 2.5 Å over the range 3700–4500 Å covering the CN feature at 3883 Å, the H and K lines of calcium, Hδ, the CH G band and the 4000 Å continuum break; the other grating (R1200R 1200 line) presented a dispersion of 1.5 Å pixel^{-1} and a spectral resolution of 5.1 Å over the range 4400–5600 Å to add absorption features such as Hβ, the Mg b triplet, and two iron lines near 5300 Å. Then, Perrett et al. (2002) calculated 12 absorption-line indices based on the prescription of Brodie & Huchra (1990). By comparing the line indices with the published M31 GC [Fe/H] values from the previous literature (Bonoli et al. 1987; Brodie & Huchra 1990; Barmby et al. 2000), the results of linear fits were obtained. Final cluster metallicities were determined from an unweighted mean of the [Fe/H] values calculated from the CH (G), Mg b, and Fe53 line strengths. For B037, Perrett et al. (2002) obtained its metallicity to be $[\mathrm{Fe/H}] = -1.07 \pm 0.20$. It is clear that B037 has a low metallicity. So, it is important to consider where the dust lane comes from.

In this paper, using the deep observations and high spatial resolution images from the ACS/*HST*, we first present that the GC B037 in M31 is crossed by a dust lane. Photometric data in the F606W and F814W bands demonstrate that colors of $(\mathrm{F606W} - \mathrm{F814W})$ in the dust lane are redder than ones in the other regions of B037 by ~ 0.4 mag. From the *HST* images, this dust lane seems to be contained in B037, not from the Milky Way. However, the formation of dust requires gas with a rather high metallicity. So, it seems impossible that the observed dust lane is physically associated with B037 itself, which has a low metallicity of $[\mathrm{Fe/H}] = -1.07 \pm 0.20$ given by Perrett et al. (2002). So, whether the observed dust lane in the view of B037 is from B037 itself or from the Milky Way needs to be confirmed in the future. In addition, based on these images, we present the precise variation of ellipticity and position angle, and of surface brightness profile, and determine the structural parameters of B037 by fitting a single-mass isotropic King model.

Acknowledgements I am indebted to Daming Chen, Zhou Fan, Tianmeng Zhang and Song Wang for their help in finishing this paper. I am also grateful to the referee for the important comments. This work was supported by the National Natural Science Foundation of China (Grant Nos. 10873016 and 10633020), and by the National Basic Research Program of China (973 Program), No. 2007CB815403.

References

Barmby, P., Holland, S., & Huchra, J. P. 2002a, AJ, 123, 1937
Barmby, P., Huchra, J. P., Brodie, J. P., et al. 2000, AJ, 119, 727
Barmby, P., McLaughlin, D. E., Harris, W. E., Harris, G. L. H., & Forbes, D. A. 2007, AJ, 133, 2764
Barmby, P., Perrett, K. M., & Bridges, T. J. 2002b, MNRAS, 329, 461
Battistini, P., Bonoli, F., Braccesi, A., et al. 1987, A&AS, 67, 447
Bonoli, F., Delpino, F., Federici, L., & Fusi Pecci, F. 1987, A&A, 185, 25
Brodie, J. P., & Huchra, J. P. 1990, ApJ, 362, 503
Cardelli, J. A., Clayton, G. C., & Mathis, J. S. 1989, ApJ, 345, 245
Crampton, D., Cowley, A. P., Schade, D., & Chayer, P. 1985, ApJ, 288, 494
Fan, Z., Ma, J., de Grijs, R., & Zhou, X. 2008, MNRAS, 385, 1973

Galleti, S., Bellazzini, M., Federici, L., Buzzoni, A., & Fusi Pecci, F. 2007, A&A, 471, 127
Galleti, S., Federici, L., Bellazzini, M., Buzzoni, A., & Fusi Pecci, F. 2006, A&A, 456, 985
Galleti, S., Federici, L., Bellazzini, M., Fusi Pecci, F., & Macrina, S. 2004, A&A, 416, 917
Harris, W. E., Harris, G. L. H., Holland, S. T., & McLaughlin, D. E. 2002, AJ, 124, 1435
Hubble, E. 1932, ApJ, 76, 44
Huchra, J. P., Brodie, J. P., & Kent, S. M. 1991, ApJ, 370, 495
King, I. 1962, AJ, 67, 471
King, I. R. 1966, AJ, 71, 64
Kron, G. E., & Mayall, N. U. 1960, AJ, 65, 581
Larsen, S. S., Brodie, J. P., Sarajedini, A., & Huchra, J. P. 2002, AJ, 124, 2615
Ma, J., de Grijs, R., Chen, D., et al. 2007, MNRAS, 376, 1621
Ma, J., de Grijs, R., Yang, Y., et al. 2006a, MNRAS, 368, 1443
Ma, J., van den Bergh, S., Wu, H., et al. 2006b, ApJ, 636, L93
Mackey, A. D., & van den Bergh, S. 2005, MNRAS, 360, 631
McLaughlin, D. E., Barmby, P., Harris, W. E., Forbes, D. A., & Harris, G. L. H. 2008, MNRAS, 384, 563
McLaughlin, D. E., & van der Marel, R. P. 2005, ApJS, 161, 304
Meylan, G., & Heggie, D. C. 1997, A&A Rev., 8, 1
Meylan, G., Sarajedini, A., Jablonka, P., et al. 2001, AJ, 122, 830
Michie, R. W. 1963, MNRAS, 125, 127
Perrett, K. M., Bridges, T. J., Hanes, D. A., et al. 2002, AJ, 123, 2490
Sirianni, M., Jee, M. J., Benítez, N., et al. 2005, PASP, 117, 1049
Stetson, P. B. 1987, PASP, 99, 191
van den Bergh, S. 1968, The Observatory, 88, 168
Vetešnik, M. 1962a, Bulletin of the Astronomical Institutes of Czechoslovakia, 13, 218
Vetešnik, M. 1962b, Bulletin of the Astronomical Institutes of Czechoslovakia, 13, 180